Control and single-shot readout of an ion embedded in a nanophotonic cavity

https://doi.org/10.1038/s41586-020-2160-9

Received: 22 August 2019

Accepted: 20 January 2020

Published online: 30 March 2020

Check for updates

Jonathan M. Kindem[1,2,3,4,5,6], Andrei Ruskuc[1,2,3], John G. Bartholomew[1,2,3,7], Jake Rochman[1,2,3], Yan Qi Huan[1,2,3,8] & Andrei Faraon[1,2,3]✉

Distributing entanglement over long distances using optical networks is an intriguing macroscopic quantum phenomenon with applications in quantum systems for advanced computing and secure communication[1,2]. Building quantum networks requires scalable quantum light–matter interfaces[1] based on atoms[3], ions[4] or other optically addressable qubits. Solid-state emitters[5], such as quantum dots and defects in diamond or silicon carbide[6–10], have emerged as promising candidates for such interfaces. So far, it has not been possible to scale up these systems, motivating the development of alternative platforms. A central challenge is identifying emitters that exhibit coherent optical and spin transitions while coupled to photonic cavities that enhance the light–matter interaction and channel emission into optical fibres. Rare-earth ions in crystals are known to have highly coherent $4f$–$4f$ optical and spin transitions suited to quantum storage and transduction[11–15], but only recently have single rare-earth ions been isolated[16,17] and coupled to nanocavities[18,19]. The crucial next steps towards using single rare-earth ions for quantum networks are realizing long spin coherence and single-shot readout in photonic resonators. Here we demonstrate spin initialization, coherent optical and spin manipulation, and high-fidelity single-shot optical readout of the hyperfine spin state of single $^{171}Yb^{3+}$ ions coupled to a nanophotonic cavity fabricated in an yttrium orthovanadate host crystal. These ions have optical and spin transitions that are first-order insensitive to magnetic field fluctuations, enabling optical linewidths of less than one megahertz and spin coherence times exceeding thirty milliseconds for cavity-coupled ions, even at temperatures greater than one kelvin. The cavity-enhanced optical emission rate facilitates efficient spin initialization and single-shot readout with conditional fidelity greater than 95 per cent. These results showcase a solid-state platform based on single coherent rare-earth ions for the future quantum internet.

This work is enabled by the unique properties of $^{171}Yb^{3+}$, the only paramagnetic rare-earth isotope with a nuclear spin of ½, which provides a favourable combination of a simple hyperfine structure that can be used as a qubit and clock transitions with long coherence times. Furthermore, in the crystal host yttrium orthovanadate (YVO_4 or YVO), $^{171}Yb^{3+}$ directly substitutes for Y^{3+} in a site that has non-polar symmetry (D_{2d}), which results in no first-order d.c. Stark effect and thus reduces the sensitivity to electric field fluctuations that can cause optical decoherence. The relevant energy-level structure of $^{171}Yb^{3+}$ in YVO is shown in Fig. 1a (see Supplementary Fig. 2 and ref. [20] for additional details). At zero applied magnetic field, the hyperfine interaction partially lifts the degeneracy of the ground state $^2F_{7/2}(0)$, leading to coupled electron–nuclear spin states of the form

$$|0\rangle_g = \frac{|\downarrow\Uparrow\rangle - |\uparrow\Downarrow\rangle}{\sqrt{2}},\ |1\rangle_g = \frac{|\downarrow\Uparrow\rangle + |\uparrow\Downarrow\rangle}{\sqrt{2}} \text{ and } |\text{aux}\rangle_g = |\uparrow\Uparrow\rangle, |\downarrow\Downarrow\rangle$$

Here we denote the electron spin as $|\uparrow\rangle = |S_z = \frac{1}{2}\rangle$ and $|\downarrow\rangle = |S_z = -\frac{1}{2}\rangle$, and the nuclear spin as $|\Uparrow\rangle = |I_z = \frac{1}{2}\rangle$ and $|\Downarrow\rangle = |I_z = -\frac{1}{2}\rangle$. We use the ground states $|0\rangle_g$ and $|1\rangle_g$, which are separated by about 675 MHz, to form the spin qubit. The $|0\rangle_g$ and $|1\rangle_g$ states have zero net magnetic moment and as a result the $|0\rangle_g \leftrightarrow |1\rangle_g$ transition is first-order insensitive to magnetic fluctuations that induce decoherence[12,21]. The $|0\rangle_g \leftrightarrow |1\rangle_g$ transition retains the strength of an electron spin transition, which enables fast and efficient microwave manipulation.

A typical experimental sequence with spin initialization, control and readout is shown in Fig. 1b. The $^{171}Yb^{3+}$ ions are coupled to a photonic

[1]Thomas J. Watson, Sr, Laboratory of Applied Physics, California Institute of Technology, Pasadena, CA, USA. [2]Kavli Nanoscience Institute, California Institute of Technology, Pasadena, CA, USA. [3]Institute for Quantum Information and Matter, California Institute of Technology, Pasadena, CA, USA. [4]Present address: JILA, University of Colorado, Boulder, CO, USA. [5]Present address: National Institute of Standards and Technology, Boulder, CO, USA. [6]Present address: Department of Physics, University of Colorado, Boulder, CO, USA. [7]Present address: School of Physics, The University of Sydney, Sydney, New South Wales, Australia. [8]Present address: Institute of Materials Research and Engineering (IMRE), Agency for Science, Technology and Research (A*STAR), Singapore, Singapore. ✉e-mail: faraon@caltech.edu

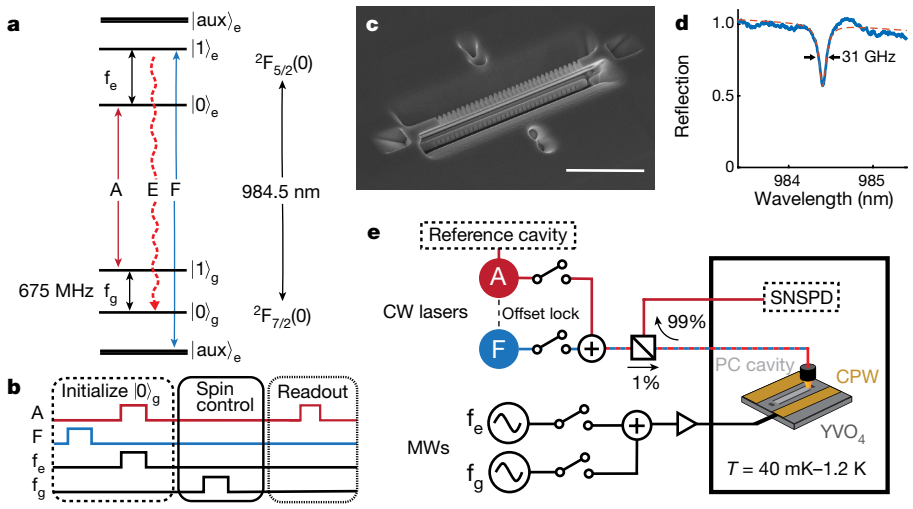

Fig. 1 | Experimental platform. a, Zero-field energy level structure of $^{171}Yb^{3+}$:YVO. States $|0\rangle_g$ and $|1\rangle_g$ form the spin qubit. Red transitions A and E are coupled (co-polarized) to the cavity, while the blue transition F is cross-polarized to the cavity mode. **b**, Typical experimental sequence used to initialize the ion into the $|0\rangle_g$ state, manipulate the qubit and optically read out the spin state. **c**, Scanning electron microscope image of a photonic crystal cavity fabricated in YVO. Scale bar, 10 μm. **d**, Reflection spectrum of the cavity. **e**, Schematic of the experimental setup. The optical transitions are addressed using pulses generated from two frequency-stabilized continuous-wave (CW) lasers. The qubit is directly manipulated using microwave (MW) control pulses using a coplanar waveguide (CPW) next to the photonic crystal (PC) cavity, which is mounted in a dilution refrigerator. Light collected from the cavity is detected using a superconducting nanowire single-photon detector (SNSPD).

crystal cavity with a large quality factor ($Q \approx 1 \times 10^4$; Fig. 1c, d, Methods) and a small mode volume of about $1(\lambda/n_{YVO})^3$, where λ is the wavelength of the optical transition and n_{YVO} is the refractive index of YVO. This enhances the emission rate, collection efficiency and cyclicity of the optical transitions A and E via the Purcell effect[22]. The qubit is initialized into the $|0\rangle_g$ state by optical and microwave pumping on the F, A and f_e transitions to empty the $|aux\rangle_g$ and $|1\rangle_g$ states, followed by cavity-enhanced decay into the $|0\rangle_g$ state via transition E (Fig. 1a). A subsequent microwave π pulse applied on the f_g transition optionally initializes the ion into the $|1\rangle_g$ state. The $|1\rangle_g$ state population is read out by excitation on the A transition and collection of the resulting ion fluorescence. Measurements are performed in a cryostat at 40 mK unless mentioned otherwise (see Methods for discussion of sample temperature). The ions are optically addressed using two frequency-stabilized continuous-wave lasers, while a microwave coplanar waveguide allows for driving of the spin transitions (Fig. 1e).

The YVO material used has a residual concentration of $^{171}Yb^{3+}$ of approximately 20 parts per billion (ppb) that is distributed over an optical inhomogeneous linewidth of about 200 MHz in the device due to variations in the local crystalline environment. This enables frequency isolation of single ions via pulsed resonant photoluminescence excitation (PLE) spectroscopy on transition A. The PLE scan in Fig. 2a (see also Extended Data Fig. 1) shows peaks in fluorescence that are confirmed to originate from single ions by measuring the pulse-wise second-order photon correlation, $g^{(2)}(t)$, of the resonant emission (Fig. 2b). For ion X (marked in Fig. 2a), $g^{(2)}(0) = 0.15 \pm 0.01$ (±s.d.). The observed bunching behaviour for time $t > 0$ is expected for a multilevel system with long-lived shelving states (Supplementary Section 2.3). An optical lifetime of $T_1 = 2.27$ μs is measured for ion X (Fig. 2c), which is a reduction from the bulk lifetime (267 μs) by $\beta F_p = 117$ (where $\beta = 0.35$ is the branching ratio for emission via transition A and F_p is the Purcell factor for the cavity-coupled transition) and corresponds to a single-photon coupling rate of $g = 2\pi \times 23$ MHz. Similar measurements were performed on the ion marked as Y in Fig. 2a (Supplementary Section 2).

The cavity-enhanced optical transitions enable coherent optical control and efficient spin initialization (Methods, Extended Data Fig. 2). Measurements of the resonant photoluminescence with varying excitation pulse length show optical Rabi oscillations (Fig. 2d), enabling calibration of π and π/2 pulses for optical control and spin readout. An optical Ramsey measurement (Fig. 2e) gives a dephasing time of $T^*_{2,o} = 370 \pm 10$ ns (values are 68% confidence intervals unless otherwise noted), a factor of 12 shorter than the lifetime-limited $T_2 = 2T_1$. Furthermore, optical echo measurements give a coherence time of $T_{2,o} = 4.1 \pm 0.2$ μs (Extended Data Fig. 3a), which implies that $T^*_{2,o}$ is limited by quasi-static fluctuations of the transition frequency. We currently attribute these fluctuations to second-order sensitivity to magnetic and electric fields (Supplementary Section 4). However, a residual first-order sensitivity to electric fields could arise from a reduction of the site symmetry due to strain, which would also lead to the observed splitting of the $|aux\rangle_g$ state at zero field (Supplementary Fig. 3). Additional measurements show these optical properties are preserved up to temperatures of 1 K (Supplementary Fig. 6). We can extend the $T^*_{2,o}$ beyond 1 μs by using post-selection to ensure the ion is on resonance with the readout sequence (Extended Data Fig. 3b, c). We measure the long-term stability, or equivalently the spectral diffusion, of the ion using PLE readout over 6 h (Fig. 2f) and observe a narrow integrated linewidth of 1.38 ± 0.03 MHz (full-width at half-maximum).

We use this optical initialization and detection to demonstrate coherent spin manipulation by driving Rabi oscillations on the $|0\rangle_g \leftrightarrow |1\rangle_g$ qubit transition (Fig. 3a). We perform a spin Ramsey measurement to extract a spin dephasing time of $T^*_{2,s} = 8.2 \pm 0.7$ μs (Fig. 3b), which is consistent with the linewidth measured with optically detected magnetic resonance (Supplementary Fig. 7) and predicted by the superhyperfine interaction with neighbouring host nuclei (Supplementary Section 5.1). The spin coherence is further extended using dynamical decoupling sequences[23] to suppress quasi-static contributions to dephasing. Figure 3c shows the resulting coherence decay for increasing numbers of π pulses using a Carr-Purcell-Meiboom-Gill (CPMG) sequence (Fig. 3c, inset). For a single π pulse, or spin echo sequence, we observe non-exponential behaviour characteristic of a spin coupled to a slowly fluctuating dipolar spin-bath[24,25] with $T_{2,s} = 44 \pm 2$ μs. This is further evidenced by a measurement of the coherence time with N, the number of π pulses, which scales as $N^{0.70 \pm 0.01}$ (Extended Data Fig. 4a, Supplementary Section 5.3). CPMG scans taken with finer temporal resolution reveal periodic collapses and revivals of coherence indicative of coupling to nearby nuclear spins (Extended Data Fig. 4b) that could potentially be used as local quantum registers.

We explore the limits of the spin coherence time by increasing the number of rephasing pulses with a fixed pulse separation of 5.74 μs to avoid unwanted interactions with the nuclear spin bath[26]. This enables extension of the CPMG coherence time to 31 ± 3 ms (Fig. 3d). While the CPMG sequence does not allow for preservation of arbitrary quantum states, we also demonstrate coherence times longer than 4 ms using an XY-8 sequence[23] (Supplementary Fig. 9) suitable for use in long-range quantum networks[27]. The measured spin-state lifetime of 54 ± 5 ms (Extended Data Fig. 5) indicates that the observed coherences are approaching the lifetime limit. We repeated these measurements at cryostat temperatures up to 1.2 K (Fig. 3d) and observed minimal changes in the spin coherence and lifetime,

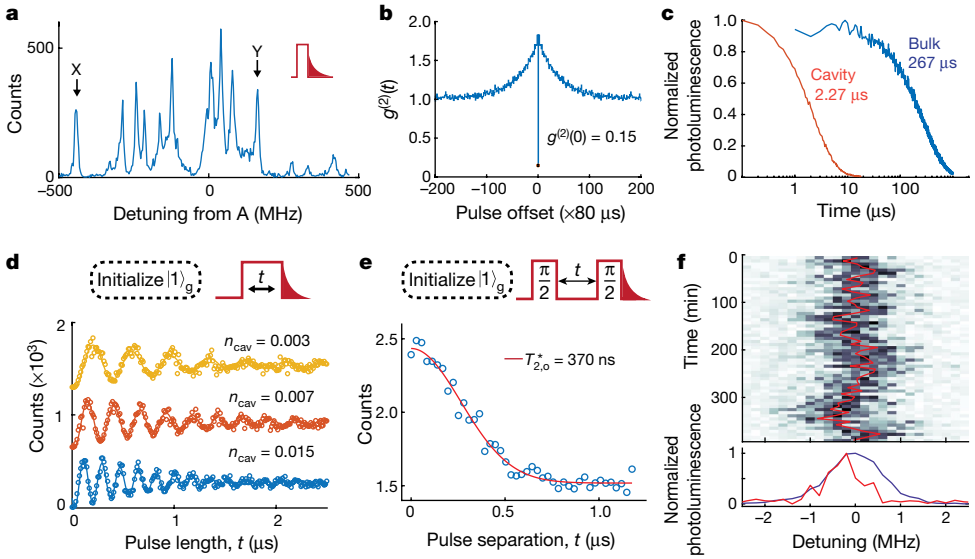

Fig. 2 | Optical detection and coherent optical manipulation of single $^{171}Yb^{3+}$ ions. a, PLE spectrum showing resolved peaks corresponding to single $^{171}Yb^{3+}$ ions. **b**, Pulsed autocorrelation measurement on ion X with $g^{(2)}(0) = 0.15 \pm 0.01$. **c**, Normalized photoluminescence emission from ion X coupled to the cavity (red) compared with typical photoluminescence from ions in bulk crystal (blue) showing a lifetime reduction of about 120. **d**, Optical Rabi oscillations on transition A after initialization into state $|1\rangle_g$. The resulting fluorescence is plotted versus pulse length for different average cavity photon number n_{cav}. Plots are offset for clarity. **e**, Optical Ramsey measurement on transition A, indicating a dephasing time $T^*_{2,o} = 370 \pm 10$ ns. **f**, Measurement of spectral diffusion over 6 h in which we repeatedly measure the transition frequency using PLE. Bottom plot shows typical scan (red) and sum of counts acquired during all scans (black), which is fitted to a Gaussian with full-width at half-maximum of 1.38 ± 0.03 MHz.

providing evidence that they are not limited by spin-lattice relaxation (Supplementary Section 5.4). Further improvements to the spin coherence and lifetimes could be achieved by reducing spin–spin interactions through control and initialization of neighbouring spins and nuclei[28].

To harness this long spin coherence time for quantum networks, it is essential to read out the qubit state in a single measurement. We achieve this with the scheme shown in Fig. 4a, which consists of two consecutive optical read periods on transition A separated by a microwave π pulse to invert the qubit population. This scheme was designed considering that in this device, direct resonant photoluminescence readout of the qubit state can only be performed using a series of optical π pulses on transition A (Methods). The Purcell-enhanced cyclicity of transition A ($\beta_{\parallel}^{cav} > 99.6\%$; Supplementary Fig. 5) allows for multiple photon-emitting cycles before the ion is optically pumped out of the qubit subspace into $|aux\rangle_g$ ($|0\rangle_e \rightarrow |0\rangle_g$ is forbidden at zero field). Figure 4b shows the measured photon count distribution in the two readout sequences for the ion initialized in the $|0\rangle_g$ (blue) or $|1\rangle_g$ (red) states. We assign the ion to the $|1\rangle_g$ state if we measure one or more photons during the first readout sequence and zero photons during the second readout sequence, and vice versa for the $|0\rangle_g$ state. This conditional readout approach helps mitigate the effect of photon loss in the detection path, which currently limits the fidelity of readout using a single series of pulses (Supplementary Section 6.1). In addition, this method discriminates between the $|0\rangle_g$ and $|aux\rangle_g$ states to ensure that the ion is in the qubit subspace before the measurement. By implementing this scheme, we achieve an average conditional readout fidelity of $F_{avg,c} = (F_{1,c} + F_{0,c})/2 = (95.3 \pm 0.2)\%$ (±s.d.) (Fig. 4c, Supplementary Section 6).

These measurements highlight single $^{171}Yb^{3+}$ ions in YVO as a promising system for solid-state quantum networking technologies. The measured spin coherence times correspond to light propagation for thousands of kilometres in optical fibres, which is necessary for

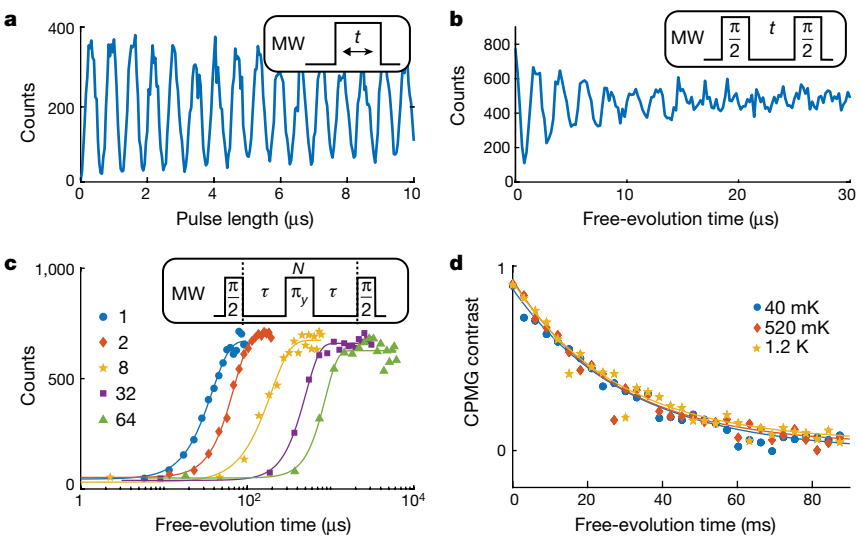

Fig. 3 | Coherent spin state control of a single $^{171}Yb^{3+}$ ion. a, Typical Rabi oscillations on the $|0\rangle_g \leftrightarrow |1\rangle_g$ microwave transition. **b**, Ramsey measurement on qubit transition (inset) that gives $T^*_{2,s} = 8.2 \pm 0.7$ μs. The excitation is detuned by 400 kHz to give rise to oscillations on the free-induction decay. **c**, Measurement of CPMG spin-coherence with increasing number of rephasing pulses, N. **d**, Measurement of spin coherence times up to 31 ± 3 ms at temperatures up to 1.2 K using CPMG with fixed pulse separation and increasing numbers of rephasing pulses.

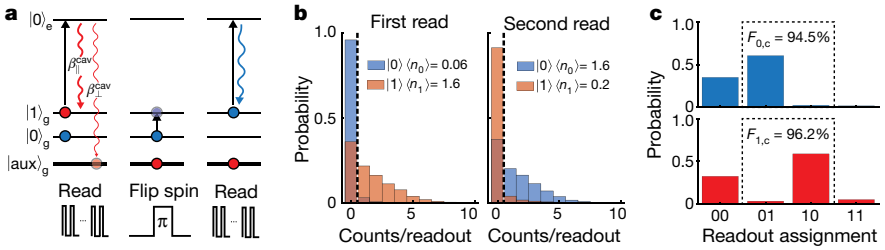

Fig. 4 | Single-shot readout of single $^{171}Yb^{3+}$ spin state. a, Scheme for single-shot readout. The ion is repeatedly excited using optical π pulses on transition A and the resulting fluorescence is collected. An ion in state $|1\rangle_g$ (red) will return to $|1\rangle_g$ with a branching ratio $\beta_{\parallel}^{cav}$ before eventually being pumped to the $|aux\rangle_g$ state, while the ion in the $|0\rangle_g$ state (blue) will be largely unaffected by the readout. A microwave π pulse is then applied to the spin transition to invert the population of $|0\rangle_g$ and $|1\rangle_g$ and the ion is optically read out again. The state of the ion is assigned based on the number of photons detected in the first and second read sequences. **b**, Photon-count distributions for the first and second read sequence used in the single-shot readout protocol with the ion initially prepared in the $|0\rangle_g$ (blue) or $|1\rangle_g$ (red) states. The dashed line shows the state assignment threshold (one photon). **c**, Distribution of assigned states *i* and *j* for the dual readout scheme with the ion initially prepared in the $|0\rangle_g$ (blue) or $|1\rangle_g$ (red) states, where *i* (*j*) is the state assigned on the first (second) read sequence. By conditioning the state of the ion on the detection of 01 or 10, we obtain an average conditional fidelity ($F_{avg,c}$) of (95.3 ± 0.2)%.

long-distance quantum networks. Furthermore, the preservation of optical and spin coherence times at temperatures of 1 K is important for developing a viable technology with economical ^{4}He cryogenics. Distributing entanglement across large-scale networks will rely on the ability to generate spin–spin entanglement and perform multi-qubit gates. Generating spin–spin entanglement with the current optical dephasing times will require a post-selection protocol similar to what has already been developed for other quantum networks[29] (Supplementary Section 4, Extended Data Fig. 3). While the source of the optical dephasing is still under investigation, it will probably be improved in higher-purity samples. The next steps are increasing the cavity quality-factor-to-mode-volume ratio by an order of magnitude to enable transform-limited photon emission and optimizing the photon collection efficiency (Supplementary Section 1). This could realistically be achieved with the current device architecture, or by using a hybrid platform where cavities are fabricated in a high-index material such as gallium arsenide and bonded to the YVO substrate. Multiqubit gates could be performed using the interaction with neighbouring vanadium ions or other rare-earth ions[30]. The technology demonstrated here with single rare-earth ion qubits complements other capabilities that could potentially be realized with $^{171}Yb^{3+}$:YVO, including quantum memories[31] for synchronizing photon traffic and quantum transducers[14,32] for coupling to qubits operating at microwave frequencies, thus pointing to a unified platform for the future quantum internet.

Note: While completing this manuscript, we became aware of a related publication on single erbium ions showing results related to those presented in Fig. 4[33].

Online content

Any methods, additional references, Nature Research reporting summaries, source data, extended data, supplementary information, acknowledgements, peer review information; details of author contributions and competing interests; and statements of data and code availability are available at https://doi.org/10.1038/s41586-020-2160-9.

1. Kimble, H. J. The quantum internet. *Nature* **453**, 1023–1030 (2008).
2. Wehner, S., Elkouss, D. & Hanson, R. Quantum internet: a vision for the road ahead. *Science* **362**, eaam9288 (2018).
3. Reiserer, A. & Rempe, G. Cavity-based quantum networks with single atoms and optical photons. *Rev. Mod. Phys.* **87**, 1379–1418 (2015).
4. Duan, L. M. & Monroe, C. Colloquium: quantum networks with trapped ions. *Rev. Mod. Phys.* **82**, 1209–1224 (2010).
5. Awschalom, D. D., Hanson, R., Wrachtrup, J. & Zhou, B. B. Quantum technologies with optically interfaced solid-state spins. *Nat. Photon.* **12**, 516–527 (2018).
6. Hensen, B. et al. Loophole-free Bell inequality violation using electron spins separated by 1.3 kilometres. *Nature* **526**, 682–686 (2015).
7. Koehl, W. F., Buckley, B. B., Heremans, F. J., Calusine, G. & Awschalom, D. D. Room temperature coherent control of defect spin qubits in silicon carbide. *Nature* **479**, 84–87 (2011).
8. Sun, S., Kim, H., Luo, Z., Solomon, G. S. & Waks, E. A single-photon switch and transistor enabled by a solid-state quantum memory. *Science* **361**, 57–60 (2018).
9. Sipahigil, A. et al. An integrated diamond nanophotonics platform for quantum-optical networks. *Science* **354**, 847–850 (2016).
10. Nguyen, C. T. et al. Quantum network nodes based on diamond qubits with an efficient nanophotonic interface. *Phys. Rev. Lett.* **123**, 183602 (2019).
11. Zhong, M. et al. Optically addressable nuclear spins in a solid with a six-hour coherence time. *Nature* **517**, 177–180 (2015).
12. Ortu, A. et al. Simultaneous coherence enhancement of optical and microwave transitions in solid-state electronic spins. *Nat. Mater.* **17**, 671–675 (2018).
13. Hedges, M. P., Longdell, J. J., Li, Y. & Sellars, M. J. Efficient quantum memory for light. *Nature* **465**, 1052–1056 (2010).
14. Williamson, L. A., Chen, Y.-H. & Longdell, J. J. Magneto-optic modulator with unit quantum efficiency. *Phys. Rev. Lett.* **113**, 203601 (2014).
15. Kutluer, K. et al. Time entanglement between a photon and a spin wave in a multimode solid-state quantum memory. *Phys. Rev. Lett.* **123**, 030501 (2019).
16. Kolesov, R. et al. Optical detection of a single rare-earth ion in a crystal. *Nat. Commun.* **3**, 1029 (2012).
17. Utikal, T. et al. Spectroscopic detection and state preparation of a single praseodymium ion in a crystal. *Nat. Commun.* **5**, 3627 (2014).
18. Zhong, T. et al. Optically addressing single rare-earth ions in a nanophotonic cavity. *Phys. Rev. Lett.* **121**, 183603 (2018).
19. Dibos, A. M., Raha, M., Phenicie, C. M. & Thompson, J. D. Atomic source of single photons in the telecom band. *Phys. Rev. Lett.* **120**, 243601 (2018).
20. Kindem, J. M. et al. Characterization of $^{171}Yb^{3+}$:YVO_4 for photonic quantum technologies. *Phys. Rev. B* **80**, 1–10 (2018).
21. Businger, M. et al. Optical spin-wave storage in a solid-state hybridized electron–nuclear spin ensemble. *Phys. Rev. Lett.* **124**, 053606 (2020)
22. Purcell, E. M. Spontaneous emission probabilities at radio frequencies. *Phys. Rev.* **69**, 681 (1946).
23. Suter, D. & Álvarez, G. A. Colloquium: protecting quantum information against environmental noise. *Rev. Mod. Phys.* **88**, 041001 (2016).
24. de Lange, G., Wang, Z., Riste, S., Dobrovitski, V. V. & Hanson, R. Universal dynamical decoupling of a single solid-state spin from a spin bath. *Science* **330**, 60–63 (2010).
25. Klauder, J. R. & Anderson, P. W. Spectral diffusion decay in spin resonance experiments. *Phys. Rev.* **125**, 912–932 (1961).
26. Abobeih, M. H. et al. One-second coherence for a single electron spin coupled to a multi-qubit nuclear-spin environment. *Nat. Commun.* **9**, 2552 (2018).
27. Humphreys, P. C. et al. Deterministic delivery of remote entanglement on a quantum network. *Nature* **558**, 268–273 (2018); correction **562**, E2 (2018).
28. Welinski, S. et al. Coherence time extension by large scale optical spin polarization in a rare-earth doped crystal. Preprint at https://arxiv.org/abs/1910.07907 (2019).
29. Bernien, H. et al. Heralded entanglement between solid-state qubits separated by three metres. *Nature* **497**, 86–90 (2013).
30. Zhong, M., Ahlefeldt, R. L. & Sellars, M. J. Quantum information processing using frozen core Y^{3+} spins in Eu^{3+}:Y_2SiO_5. *New J. Phys.* **21**, 033019 (2019).
31. Zhong, T. et al. Nanophotonic rare-earth quantum memory with optically controlled retrieval. *Science* **357**, 1392–1395 (2017).
32. Bartholomew, J. G. et al. On-chip coherent microwave-to-optical transduction mediated by ytterbium in YVO_4. Preprint at http://arxiv.org/abs/1912.03671 (2019).
33. Raha, M. et al. Optical quantum nondemolition measurement of a solid-state spin without a cycling transition. Preprint at http://arxiv.org/abs/1907.09992 (2019).

Methods

Fabrication of nanophotonic cavities in YVO

Nanophotonic cavities are fabricated directly in a YVO crystal using focused-ion-beam milling (Fig. 1c). Periodic trenches are made in a triangular nanobeam to form a photonic bandgap with the spacing of these cuts tapered in the middle to form the defect required for the optical cavity mode. The reflectivity of one side of the cavity is lowered by reducing the number of photonic crystal lattice periods to enhance the efficiency of coupling into the collection path. Light is coupled into and out of these devices via total internal reflection using 45° couplers fabricated on both sides of the device. Further details on design and fabrication of nanocavities in YVO can be found in refs. [31,34].

Devices are fabricated in a *c*-cut sample of YVO with the electric (E) field of the fundamental transverse-magnetic mode aligned with the stronger optical dipole of Yb:YVO, which is polarized along the crystal c axis. The device used here has an energy decay rate of $\kappa = 2\pi \times 30.7$ GHz (cavity quality factor $Q \approx 1 \times 10^4$). The mode volume extracted from finite-difference time-domain simulations is $V = 0.095\ \mu m^3 \approx 1(\lambda/n_{YVO})^3$, where $n_{YVO} = 2.17$ is the refractive index of YVO for $E \| c$. The coupling efficiency from fibre into the nanobeam waveguide is determined to be about 24% by direct measurement of the reflection from the device off resonance. The coupling rate of the input mirror of the cavity, κ_{in}, is extracted from the cavity reflection spectrum (Fig. 1d) to be $\kappa_{in}/\kappa \approx 0.14$. The cavity is determined to be undercoupled by measuring the phase response using a polarization interferometer.

The sample used for this work is cut and polished from a boule of YVO grown by Gamdan Optics. While nominally undoped in the growth process, the crystal contained residual concentrations of rare-earth ions. From optical absorption measurements in bulk crystals and glow discharge mass spectrometry (EAG laboratories), the total concentration of all Yb isotopes is estimated to be 0.14 ppm. Assuming natural isotopic abundance (14.3% $^{171}Yb^{3+}$), this gives a $^{171}Yb^{3+}$ concentration of about 20 ppb, which corresponds to about 23 $^{171}Yb^{3+}$ ions within the cavity mode volume.

Experimental setup

The ions in the cavity are optically addressed using two continuous-wave lasers (M2 Solstis and Toptica DLPro). To enable repeated addressing of single ions, the lasers are stabilized to a Fabry-Perot reference cavity (Stable Laser Systems) using a standard Pound-Drever-Hall and offset-frequency lock. Pulses are generated using acousto-optic modulators and sent to the device via optical fibre. Light reflected or emitted from the device is detected by a tungsten silicide superconducting nanowire single-photon detector. The total system detection efficiency (probability of detecting a photon emitted by an ion in the cavity) is about 1%.

The device is held stationary on a copper sample mount on the mixing chamber plate of a Bluefors LD250 dilution refrigerator. Light is coupled into and out of the device from fibre using an aspheric doublet mounted on an XYZ piezo-stage (Attocube) that allows for optimization of this coupling at dilution fridge temperatures. Devices are tuned onto resonance with the ion transition of interest by nitrogen deposition. Static magnetic fields are applied to the device inside the fridge using a set of homebuilt superconducting magnets made by winding superconducting wire (SC-T48B-M-0.254mm, Supercon). These magnets are used to null stray fields and maximize the spin coherence (Supplementary Fig. 8).

A gold coplanar waveguide is fabricated next to the optical cavity to allow for microwave manipulation of the ions. The centre strip of this waveguide is 60-μm wide with a spacing of 30 μm to the ground plane. The optical device sits inside this 30-μm gap. Launching microwaves through this waveguide gives rise to an oscillating magnetic field along the crystal c axis, which enables driving of the desired transitions ($|0\rangle_g \leftrightarrow |1\rangle_g$ and $|0\rangle_e \leftrightarrow |1\rangle_e$) at zero field. The YVO chip sits inside a microwave launch board (Rogers AD1000, fabricated by Hughes Circuits) with SMP connectors on both input and output. This launch board is wire-bonded to the chip with multiple wire bonds to give additional cooling through the surface.

Microwave tones to drive the ground and excited state transitions are generated using two signal generators (Stanford Research Systems SG380). The amplitude and phase of the pulses used on the ground state transition are controlled using in-phase and quadrature (IQ) modulation driven by a fast function generator (Tektronix AWG5204). Both sources pass through a set of microwave switches (Minicircuits ZASWA-2-50DR+) that provide additional extinction. The microwave tones are then combined, amplified and sent to the device in the dilution fridge. To ensure adequate microwave power at the device for these initial measurements, minimal attenuation is used on the input coaxial lines inside the fridge with a single 20-dB attenuator on the still plate and 0-dB attenuators on the other plates.

With the full experiment loaded, the temperature of the mixing chamber plate is about 40 mK. Experiments are performed with the mixing chamber plate temperature up to 1.2 K to investigate the temperature dependence of spin and optical coherence and spin lifetime. Further measurements above this temperature have not been performed at this time as this leads to spurious dark counts and increased latching of the superconducting nanowire single-photon detectors.

Additional details on the experimental setup are provided in the Supplementary Information.

Identifying single $^{171}Yb^{3+}$ ions

Potential single ions are identified with pulsed resonant PLE scans. Extended Data Fig. 1a shows an extended PLE line scan over a 12-GHz region around the centre of the optical transition. Clusters of peaks in fluorescence correspond to the different isotopes of Yb, which have the expected transitions shown in Extended Data Fig. 1b. These PLE scans are taken with Rabi frequencies greater than 10 MHz to intentionally power-broaden the optical transitions of the ions and enable coarser and faster scans. As shown in Extended Data Fig. 1b, transition A of $^{171}Yb^{3+}$ does not spectrally overlap with optical transitions from the other isotopes, while the other cavity-coupled optical transition from the qubit subspace (transition E) overlaps with the inhomogeneous distribution of the zero-spin isotope. This makes it difficult to isolate and address single $^{171}Yb^{3+}$ ions using transition E without simultaneously exciting a large number of zero-spin ions. As a result, finer scans are performed around transition A (Fig. 2a) to identify potential $^{171}Yb^{3+}$ ions.

To determine whether an isolated peak corresponds to an $^{171}Yb^{3+}$ ion, the energy-level structure is investigated using optical pumping. The readout laser is tuned on resonance with one of these peaks and a second laser is scanned across transition F. If an observed peak corresponds to the A transition of an $^{171}Yb^{3+}$ ion, the pump laser will move population into the qubit subspace as it comes into resonance with transition F and result in an increase in counts after the readout pulse. For the ions used here, we observe a splitting of transition F at zero applied magnetic field (Supplementary Fig. 3) that could be the result of strain. See Supplementary Section 2.2 for additional discussion.

Second-order intensity correlation measurements are performed to verify that an isolated peak corresponds to emission from a single ion. In Fig. 2b, $g^{(2)}(t)$ of ion X is measured by alternating between a single initialization pulse on the C transition (Supplementary Fig. 2) and a readout pulse on transition A. The pulse-wise correlation is calculated on the counts observed after the excitation pulse on transition A. The partial initialization sequence was chosen to enable fast data collection and show $g^{(2)}(0) \ll 0.5$ to confirm the single-emitter nature of the observed signal. However, this incomplete initialization into the $|1\rangle_g$ state reduces the signal-to-background ratio and thus increases

the value of $g^{(2)}(0)$. While not explored in further detail here, we expect that $g^{(2)}(0)$ is limited by the presence of spurious background counts due to the excitation of other ions in the cavity from the initialization pulse and dark counts of the superconducting nanowire single-photon detectors. We note that because the detector deadtime is short compared with the excited state lifetime and photon rate, these measurements were performed using a single detector and by calculating a full autocorrelation. Further discussion of the bunching behaviour observed in Fig. 2b is given in Supplementary Section 2.3.

Spin initialization

The single ion is first initialized into the qubit subspace by optical pumping out of the $|\mathrm{aux}\rangle_g$ state on transition F, which consists of two 2.5-μs pulses alternating between the two split transitions from the $|\mathrm{aux}\rangle_g$ state with a total repetition rate of 100 kHz. Transition F is not enhanced by the cavity, but can be driven using light orthogonal to the cavity mode. Once in the excited state $|1\rangle_e$, the ion decays by the cavity-enhanced transition E with high probability to the $|0\rangle_g$ state. The ion is initialized within the qubit subspace by optical pumping on transition A, which consists of 2.5-μs-long pulses with a 200-kHz repetition rate. As the optical transition from $|0\rangle_e \rightarrow |0\rangle_g$ is not allowed at zero field, a microwave pulse is applied simultaneously to the excited state transition f_e during optical pumping on A to create a two-photon transition between $|1\rangle_g$ and $|1\rangle_e$. Once in $|1\rangle_e$, the ion efficiently decays to $|0\rangle_g$ by transition E with branching ratio $\beta_{\parallel}^{\mathrm{cav}}$. This sequence initializes the ion into the $|0\rangle_g$ state. To initialize into the $|1\rangle_g$ state, a microwave π pulse is applied on the ground state transition after the optical initialization sequence.

To demonstrate and assess the quality of the spin initialization scheme, the population in $|1\rangle_g$ is measured for varying lengths of the preparation sequences. Extended Data Fig. 2a shows optimization of optical pumping out of the $|\mathrm{aux}\rangle_g$ state by varying the number of pulses on the F transition while keeping the number of initialization pulses on the A and f_e transitions fixed at 100. From the observed count rate, optical branching ratio and detection efficiency, the initialization into the qubit subspace is estimated to be 95%. Extended Data Fig. 2b shows initialization into the $|1\rangle_g$ (red) or $|0\rangle_g$ (blue) states as the number of pulses on the A and f_e transitions is increased while holding the number of pulses on the F transition fixed at 150. Without any subtraction of background count contributions, a population contrast of 91% is observed, which corresponds to an initialization fidelity of 96% within the qubit subspace. This demonstrates that this pumping scheme allows for efficient initialization between these two spin states in under 500 μs. Here, the state population in $|1\rangle_g$ is measured using PLE with a series of 500 optical π pulses on transition A. The initialization measured in this way will be limited by the readout fidelity of this pulse sequence and so represents a lower bound.

Microwave control of single ions

Optically detected magnetic resonance measurements were performed on the ground state spin transition $|0\rangle_g \leftrightarrow |1\rangle_g$ for initial calibration of the spin transition frequencies and to bound the coherence time (Supplementary Section 5.1). Additional calibration of the centre frequency of the spin transition is accomplished by minimizing the frequency of Rabi oscillations as a function of microwave drive frequency. The length of microwave control pulses is extracted from the microwave Rabi oscillations. Finer calibrations of π pulse lengths are performed by initializing the ion into the $|0\rangle_g$ state, applying an even number of π pulses and minimizing the resulting population in $|1\rangle_g$ as a function of pulse length.

For the spin coherence measurements presented in Fig. 3c, the phase of the final π/2 pulse is chosen to be 180° out of phase with the initial π/2 pulse to map the coherence to the $|0\rangle_g$ state population. This gives rise to the increasing exponential decay observed in Fig. 3c. The CPMG contrast in Fig. 3d is extracted by alternating the phase of the final π/2 pulse to be in phase or 180° out of phase with the initial π/2 pulse to map the coherence to the $|1\rangle_g$ or $|0\rangle_g$ state population. The contrast is given by the normalized difference between these two readouts.

Unless otherwise specified, optical readout of the spin state for coherence and lifetime measurements is performed using a series of optical π pulses and integrating the fluorescence observed over many repetitions of the experiment.

Spin lifetime and device temperature

The lifetimes of the spin transitions are measured by initializing the ion into state $|0\rangle_g$, waiting for a period of time τ and optically reading out either the $|0\rangle_g$ or $|1\rangle_g$ population on transition A. The $|0\rangle_g$ population is measured by applying a microwave π pulse followed by optical readout on transition A. Extended Data Fig. 5 shows the results of such a measurement at a cryostat temperature of 40 mK. A biexponential decay of the $|0\rangle_g$ population is observed: a rapid decay (54 ± 5 ms) due to thermalization with state $|1\rangle_g$ (Extended Data Fig. 5a) followed by a much slower decay (26 ± 2 s) as the states $|0\rangle_g$ and $|1\rangle_g$ thermalize with $|\mathrm{aux}\rangle_g$ (Extended Data Fig. 5b). From the ratio between the $|0\rangle_g$ and $|1\rangle_g$ populations after the short $|0\rangle_g \leftrightarrow |1\rangle_g$ relaxation, we extract a device temperature of 59 ± 4 mK by assuming a Boltzmann distribution. This is in reasonable agreement with the measured mixing chamber plate temperature of 40 mK.

Single-shot readout fidelities

For single-shot readout, the state of the ion is assigned based on the number of photons detected during two optical readout periods consisting of a series of optical excitation pulses on transition A separated by a microwave π pulse on the qubit transition. The qubit is optically read out on transition A, because transition E overlaps with the optical transition of the zero-spin isotope. We choose a photon number cutoff, n_c, and during each read period assign the state of the ion to $|1\rangle_g$ if we measure n_c or more photons during the readout period and to $|0\rangle_g$ if we measure less than n_c photons. The results of this measurement are labelled as $|ab\rangle$, where a (b) is the outcome of the first (second) readout. The initial state of the ion is conditionally assigned to the $|0\rangle_g$ state on the observation of $|01\rangle$, and to the $|1\rangle_g$ state on the observation of $|10\rangle$.

To measure the photon count distributions and assign a readout fidelity, the ion is initialized into the $|0\rangle_g$ or $|1\rangle_g$ state and the readout procedure is repeated many times to acquire adequate statistics. Figure 4b shows the resulting photon count histograms in which 400 read pulses were used per sequence, showing good agreement with the expected form for the photon count distributions. Further details on readout fidelities and photon count distributions are discussed in Supplementary Section 6.

Data availability

The data that support the findings of this study are available from the corresponding author upon request.

34. Zhong, T., Rochman, J., Kindem, J. M., Miyazono, E. & Faraon, A. High quality factor nanophotonic resonators in bulk rare-earth doped crystals. *Opt. Express* **24**, 536–544 (2016).

Acknowledgements This work was funded by a National Science Foundation (NSF) Faculty Early Career Development Program (CAREER) award (1454607), the AFOSR Quantum Transduction Multidisciplinary University Research Initiative (FA9550-15-1-0029), NSF 1820790, and the Institute of Quantum Information and Matter, an NSF Physics Frontiers Center (PHY-1733907) with support from the Moore Foundation. The device nanofabrication was performed in the Kavli Nanoscience Institute at the California Institute of Technology. J.G.B. acknowledges the support from the American Australian Association's Northrop Grumman Fellowship. J.R. acknowledges the support from the Natural Sciences and Engineering Research Council of Canada (NSERC) (PGSD3-502844-2017). Y.Q.H. acknowledges the support from the Agency for Science, Technology and Research (A*STAR) and Carl & Shirley Larson as a Frederick W. Drury Jr. SURF Fellow. We thank M. Shaw, S. Woo Nam and V. Verma for help with superconducting photon detectors; A. Sipahigil for discussion; K. Schwab for help with electronics; and D. Riedel for supporting measurements.

Author contributions J.M.K., J.G.B. and A.F. conceived the experiments. J.R. fabricated the nanophotonic device. J.M.K., A.R. and J.G.B. performed the experiments and analysed the data. Y.Q.H. provided simulation support. J.M.K., A.R. and A.F. wrote the manuscript with input from all authors. A.F. supervised the project.

Competing interests The authors declare no competing interests.

Additional information
Supplementary information is available for this paper at https://doi.org/10.1038/s41586-020-2160-9.

Correspondence and requests for materials should be addressed to A.F.
Peer review information *Nature* thanks David Hunger, Andreas Reiserer and the other, anonymous, reviewer(s) for their contribution to the peer review of this work.
Reprints and permissions information is available at http://www.nature.com/reprints.

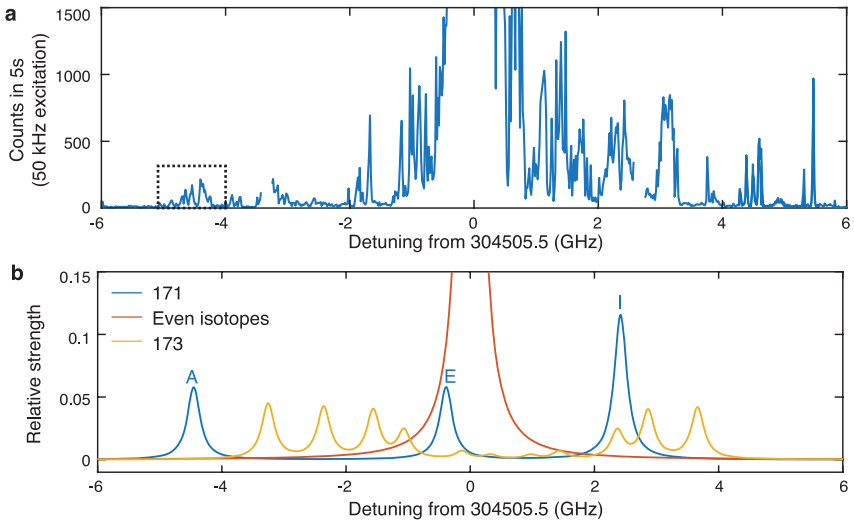

Extended Data Fig. 1 | Extended PLE scans and expected ion distribution. **a**, Photoluminescence scan over 12 GHz centred around the optical transition of the zero-nuclear-spin isotope with zero applied magnetic field. The dashed box highlights the region scanned in Fig. 2a. **b**, Predicted optical transition frequencies of the different Yb isotopes for $E||c$ with transition strength scaled to natural abundance.

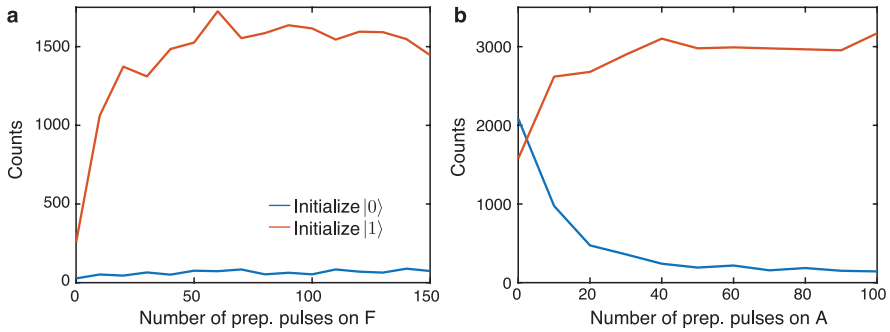

Extended Data Fig. 2 | Spin initialization. Blue (red) scans correspond to preparation into the $|0\rangle_g$ ($|1\rangle_g$) state. **a**, Initialization into qubit subspace. The number of preparation pulses on the A and f_e transitions is held fixed at 100 while the number of preparation pulses on transition F is varied. **b**, Initialization within qubit subspace. The number of preparation pulses on F is held fixed at 150 while the number of preparation pulses on transitions A and f_e is varied. The observed population contrast corresponds to an initialization fidelity of >96% within the qubit subspace.

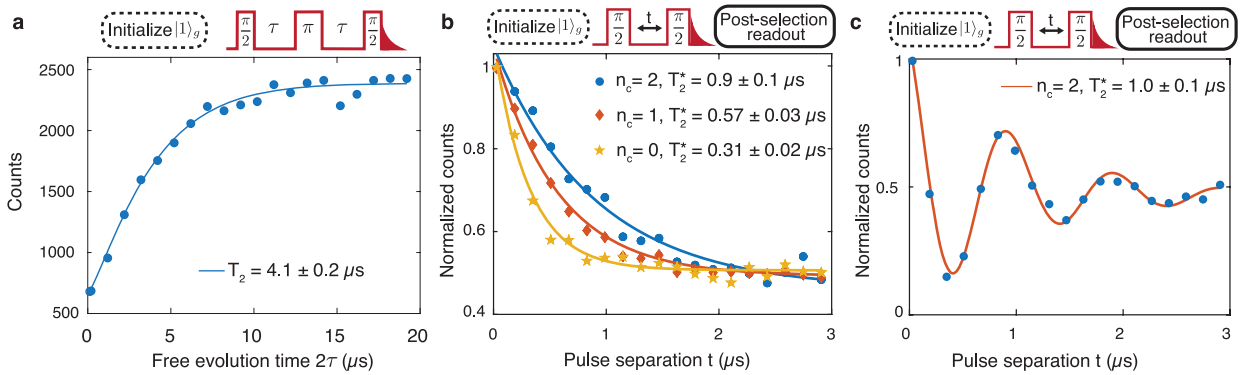

Extended Data Fig. 3 | Additional optical coherence measurements. **a**, Measurement of optical T_2 on ion Y using an echo sequence. The fit gives $T_2 = 4.1 \pm 0.2$ µs. **b**, Post-selected optical Ramsey measurement (Supplementary Section 4) with resonant excitation showing improvement in T_2^* for increasing numbers of photons n_c detected in a subsequent probe sequence. **c**, Post-selected Ramsey sequence for $n_c = 2$ with readout detuned by 1 MHz to demonstrate that decay is due to optical coherence.

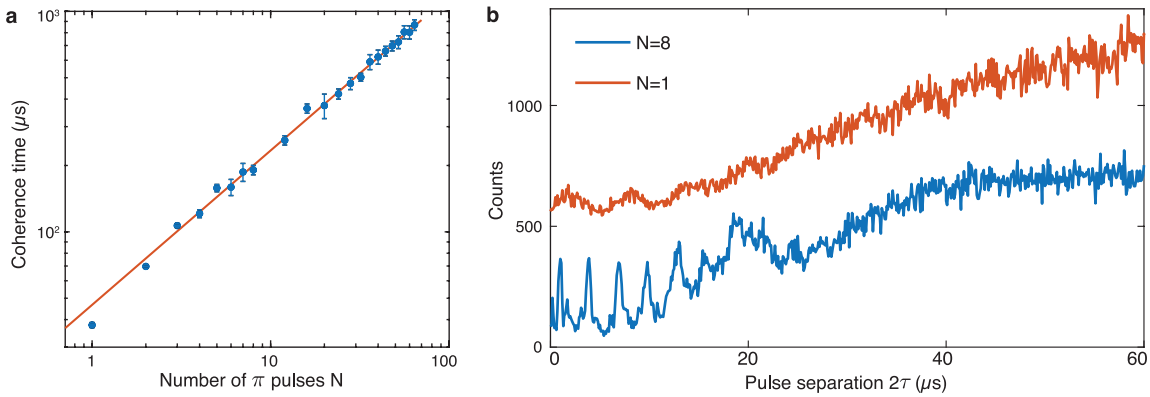

Extended Data Fig. 4 | Additional CPMG measurements. a, Scaling of coherence time extracted from CPMG envelope (Fig. 3c) for increasing numbers of rephasing pulses. Error bars represent 68% confidence intervals for CPMG coherence times. The fit gives $T_{2,s}^{N} \propto N^{0.70\pm0.01}$. **b**, Fine-resolution CPMG scans performed with $N=1$ (red) and $N=8$ (blue) rephasing pulses showing periodic collapses and revivals of the spin coherence. The $N=1$ scan is offset by 500 counts for clarity.

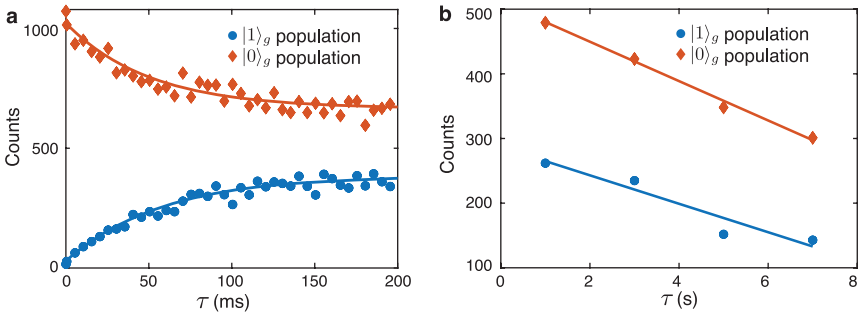

Extended Data Fig. 5 | Spin lifetime measurements. a, Measurement of population in the $|0\rangle_g$ and $|1\rangle_g$ states after initializing into the $|0\rangle_g$ state and waiting for time τ. Exponential fit gives a lifetime of 54 ± 5 ms. The measured population difference corresponds to a device temperature of 59 ± 4 mK. **b**, Slow decay of population from qubit subspace into the $|\mathrm{aux}\rangle_g$ state with decay constant 26 ± 2 s.